Published by IOP Publishing for Sissa Medialab

Received: *December 2, 2025*
Accepted: *February 19, 2026*
Published: *March 11, 2026*

Characterization of a resistive Micromegas detector with capacitive-sharing pad readout

M. Alviggi[a,b] **M. Biglietti**[c,*] **M.T. Camerlingo**[d] **K. Chmiel**[c,f] **M. Della Pietra**[a,b] **C. Di Donato**[a,e] **R. Di Nardo**[c,f] **P. Iengo**[a] **M. Iodice**[c] **R. Orlandini**[c,f] **F. Petrucci**[c,f] **G. Sekhniaidze**[a] **and M. Sessa**[a]

[a] *INFN sezione di Napoli, Napoli, Italy*
[b] *Università di Napoli Federico II, Napoli, Italy*
[c] *INFN sezione di Roma Tre, Roma, Italy*
[d] *INFN sezione di Bari, Bari, Italy*
[e] *Università di Napoli "Parthenope", Napoli, Italy*
[f] *Università Roma Tre, Roma, Italy*

E-mail: michela.biglietti@cern.ch

Abstract: We report on the performance of a resistive Micromegas detector equipped with a novel readout architecture that achieves high spatial resolution while significantly reducing the number of readout channels. The concept relies on capacitive charge sharing within a vertical stack of four pad layers embedded in a 2 mm-thick PCB. This multilayer structure distributes the signals induced by the avalanches generated in the Micromegas amplification gap across multiple pads of the anode plane, resulting in a lateral broadening of the induced signal. The extent of charge sharing is set by the pad geometry and layout in the stacks, allowing an optimal distribution of signal among neighbouring readout elements. The capacitive-sharing stack is produced with standard PCB techniques, ensuring scalability and straightforward integration. A prototype was characterized with X-rays in the laboratory and with a muon beam at the CERN Super Proton Synchrotron (SPS). It operated stably at high gain, delivered spatial resolutions of 1/20 and 1/30 of the pad pitch for 5 mm and 10 mm pads, respectively, and reached a detection efficiency of 98% at plateau with tracks perpendicular to the detector plane. The detector performance was also studied in detail for tracks incident at non-perpendicular angles (achieving efficiencies close to 100%), exploiting the timing information of the hits to refine the spatial reconstruction.

Keywords: Gaseous detectors; Micropattern gaseous detectors (MSGC, GEM, THGEM, RETHGEM, MHSP, MICROPIC, MICROMEGAS, InGrid, etc)

*Corresponding author.

https://doi.org/10.1088/1748-0221/21/03/P03017

Contents

2026 JINST 21 P03017

1 Introduction

Micro-pattern gaseous detectors (MPGDs) are having an increasing importance for particle detection in high-energy and nuclear physics experiments by offering high spatial resolution and robust performance. These detectors operate by amplifying electron signals within a finely segmented readout structure, typically composed of strips or pads. Although this segmentation improves position accuracy, double-track separation, and ensures low occupancy for high rate applications, it also introduces significant challenges for large-scale implementations, such as an increased number of electronic channels and greater integration complexity that can affect detector acceptance and performance.

Micromegas detectors are characterized by a single-stage amplification based on a parallel-plate electrode structure and have been extensively developed for high-rate applications [1–4]. A stainless steel micro-mesh divides the gas volume into a conversion (drift) gap of a few millimeters and a narrow amplification gap of about 0.1 mm, where an intense electric field (40–50 kV/cm) is applied. A resistive layer is typically added above the readout plane to mitigate the effects of sparks and discharges. The readout plane, typically composed of micro-strips or pads, collects the induced signals via capacitive coupling. The dimensions of the readout elements are optimised based on particle rates, the required spatial resolution, and the noise introduced by large capacitance.

For applications with low/moderate particle flux, a lower-granularity readout pattern can be used, which reduces the number of readout channels and therefore significantly lowers costs. However, this typically comes at the expense of spatial resolution. To restore the spatial resolution, the charge can be spread among several electrodes so that the position can be reconstructed through the charge-weighted cluster centroid [6]. Two different solutions can be exploited to spread the charge on the readout plane. One is the use of a low-resistivity layer, which spreads the charge over multiple strips or pads. However, a too low resistivity spoils the benefit of the resistive layer as spark-protection element. The other approach, which will be described in detail below, relies on charge spreading through capacitive coupling, using a stack of layers with metal pads or strips of increasing dimensions. An advantage of this solution is that a high-resistivity spark protection layer can be maintained, ensuring

stable operation. In fact, it shifts the necessary design changes to the PCB (at minimal cost) while keeping the detector in its optimised configuration.

In this paper we present the first implementation of capacitive-sharing readout structures in Micromegas detectors. This novel approach [7] enables charge transfer and sharing over large-pitch anode readout layers using capacitive coupling between stacked pad layers. Capacitive-sharing readout structures significantly enhance spatial resolution while reducing the required number of electronic channels, making them highly suitable for large-area MPGD-based tracking detectors in low and medium rate applications. An evaluation of the limits on the rate capability strongly depends on the specific configuration and on the increase in occupancy due to charge sharing. Dedicated measurements with different prototypes are planned to address this topic.

Section 2 describes the layout and structure of the first small-scale $10 \times 10\,\mathrm{cm}^2$ Micromegas prototype implementing the capacitive-sharing readout. Section 3 presents its performance from laboratory measurements, while section 4 reports on results from beam tests at CERN. Finally, section 5 provides a summary of the work and outlines future prospects.

2 Micromegas prototype with capacitive-sharing pad readout structure

A detailed description of various pixelised resistive Micromegas prototypes, along with a comparative analysis of their performance with different resistive layouts and configurations, can be found in [3] and [4]. To study the capacitive-sharing readout in Micromegas, a small $10 \times 10\,\mathrm{cm}^2$ prototype was designed and built in collaboration with the CERN Micro-Pattern Technologies (MPT) workshop.

The basic concept of the capacitive-sharing readout structure is illustrated in figure 1, which shows the cross-section of the amplification gap and the multilayer readout PCB, implementing the copper-pad layers. The pad pitch doubles from one layer to the next, thus the number of pads is reduced by a factor four at each layer. The bottommost layer in the stack is the readout layer, directly connected to the front-end amplifier ASICs of the readout electronics. Above it, the intermediate layers are stacked, which enable signal propagation via a cascade of capacitive couplings from the amplification region down to the readout. The pad layers are designed such that the geometric center of each pad in a given layer is alternately centered on a larger pad or aligned with the boundary between two adjacent larger pads in the subsequent layer. The signal propagates through the pad layers down to the readout via capacitive coupling, while simultaneously spreading laterally across pads of progressively larger size. Thanks to this design, the pad size of the internal high-granularity layer determines the spatial resolution, whereas the final readout layer, equipped with larger pads, sets the total number of electronic channels needed to read out the detector. At the top of the stack, above the first transfer layer, lies the resistive layer consisting of a thin diamond-like carbon (DLC) film sputtered onto a 50 µm thick polyimide insulating foil. The resistive layer provides spark protection and evacuates the incoming charge to ground. In figure 1, the arrow represents a charged particle traversing the detector, producing the electron charge cloud generated by the amplification gap. The red and orange pads indicate fired pads, illustrating how the charge spreads across increasingly larger neighbouring pads as it is transferred from the top layer down to the readout layer via capacitive coupling.

Figure 2 shows a picture of the small Micromegas prototype with capacitive-sharing pads under test, named Paddy-CS, and its readout pad structure together with the scheme of the routing strips from the pads to the connectors.

2026 JINST 21 P03017

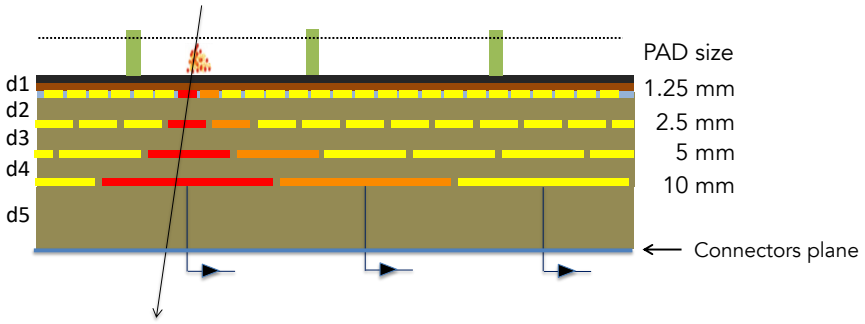

Figure 1. View of the capacitive-sharing pad readout (side-L of figure 2), illustrating the intermediate layers of $1.25 \times 1.25\,\mathrm{mm}^2$, $2.5 \times 2.5\,\mathrm{mm}^2$ and $5 \times 5\,\mathrm{mm}^2$ pads, and the readout layer at the bottom with $10 \times 10\,\mathrm{mm}^2$ pads. The black top layer represents the DLC resistive film. The detector stack-up (not to scale) has the following dimensions: d1 = d2 = 0.100 mm; d3 = 0.125 mm; d4 = 0.150 mm; d5 = 1.5 mm. All layers are interspersed with a 50 µm thick layer of glue.

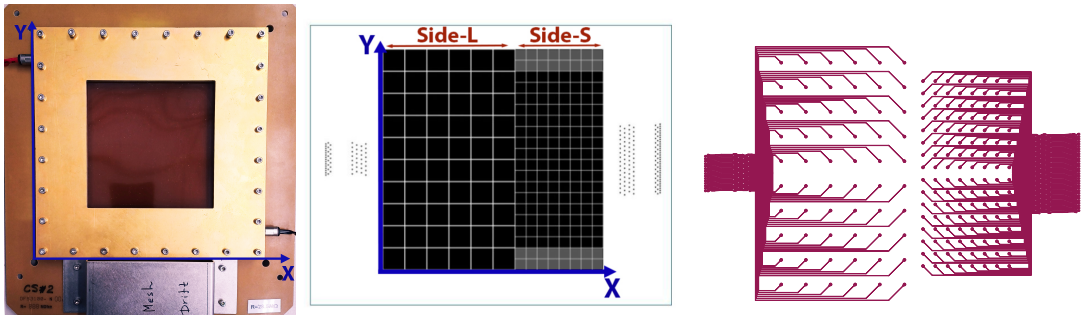

Figure 2. Photograph of the $10 \times 10\,\mathrm{cm}^2$ capacitive-sharing Micromegas prototype (left), layout of the readout pads (centre) and scheme of the routing strips from the pads to the connectors (right). The active area is divided into two sections: side-L, with $10 \times 10\,\mathrm{mm}^2$ readout pads, and Side-S, with $5 \times 5\,\mathrm{mm}^2$ readout pads. In the Side-S section, the two rows of pads at the highest and lowest Y positions (grey in the figure) are not read out, as this would have exceeded the maximum number of channels supported by the 128-channel front-end electronics.

This prototype was built to facilitate the study of two different configurations of square pads: one side with readout pads of pitch $10 \times 10\,\mathrm{mm}^2$ and the other with $5 \times 5\,\mathrm{mm}^2$. The detector features an active area of $10 \times 10\,\mathrm{cm}^2$ and is made with bulk technology [8], incorporating a standard woven stainless-steel mesh with 400 wires per inch. The mesh wire's diameter is 18 µm, with 45 µm open window between woven wires, resulting in a pitch of 63 µm. The drift gap is 5 mm while the nominal (effective) amplification gap is approximately 150 (120) µm. The anode consists of a 2 mm thick PCB implementing the capacitive layers. On top, the resistive layer consists of sputtered DLC of sub-micrometre thickness, with a resistivity of about 30 MΩ/□.

The structures of the pads in the four layers of the PCB implementing the capacitive-sharing concept are shown in figure 3. The number and side dimensions of the squared pad pitch in the four layers are as follows:

- First layer (closest to the amplification gap, where signals are induced): 81×81 pads, with a pitch of 1.25 mm.

2026 JINST 21 P03017

- Second layer (first capacitive-sharing layer): 41×41 pads, with a pitch of 2.5 mm.
- The difference between the Paddy-CS-L side and Paddy-CS-S emerges in the third layer. The Paddy-CS-L side features a matrix of 21×12 square pads with a pitch of 5 mm and a row of 21 rectangular pads (5×2.5 mm^2 wide) at the edge between Paddy-CS-S and Paddy-CS-L. The Paddy-CS-S side comprises a matrix of 20×8 square pads with 5 mm pitch.
- The prototype features two distinct readout sections in the fourth (readout) layer: one section (Paddy-CS-L) is equipped with 10×6 square readout pads of side dimension 10 mm, while the other section (Paddy-CS-S) utilizes smaller, 5 mm readout pads, maintaining the same segmentation and position with respect to previous layer.[1]

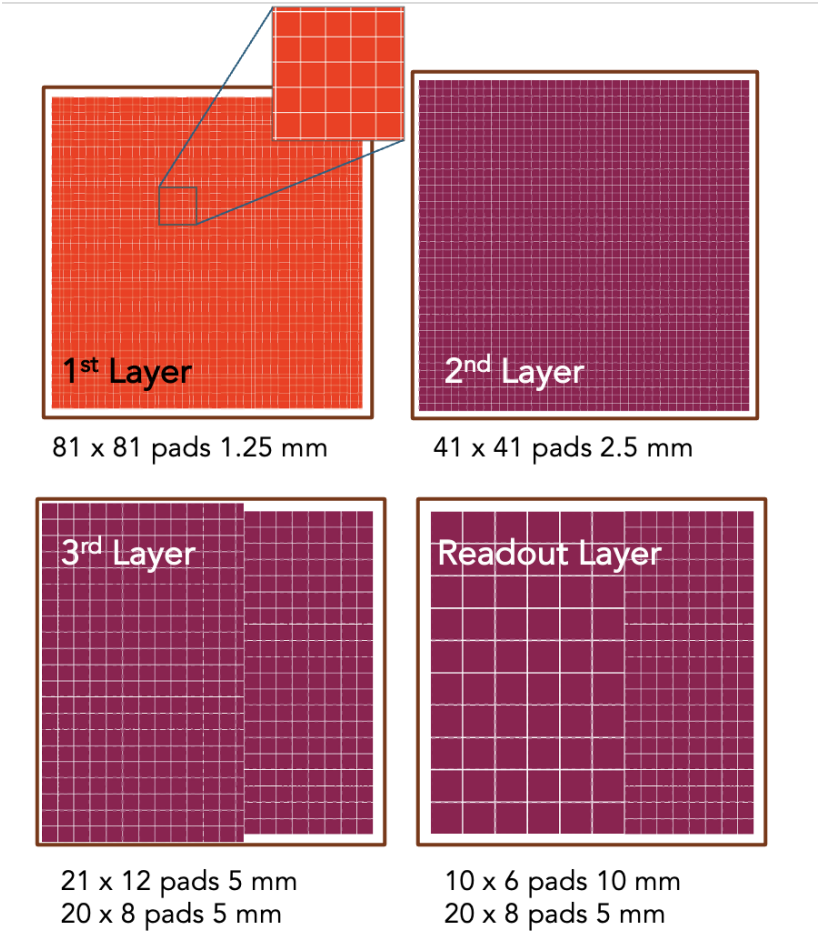

Figure 3. Structures of the pads in the four layers of the PCB implementing the capacitive-sharing concept. Note the column of 21 rectangular pads along the border that separates the two different regions in the 3rd layer (bottom left plot).

Figure 3 shows the layout of the three internal layers and the readout layer. This configuration allows for comparative studies of capacitive-sharing performance with different readout pad granularities within the same detector.

[1] Actually, the fourth layer in the CS-S layout does not operate any further charge sharing, but it is necessary to ensure the same thickness of the PCB on both halves of the same detector in order to simplify the production of the prototype.

2026 JINST 21 P03017

Compared to conventional pad-based Micromegas detectors, such as those described in [4], this prototype implements several design differences. It employs a single continuous DLC resistive layer for spark protection, instead of a double DLC layer. This spark-protection structure design simplifies the evacuation circuitry and manufacturing. Secondly, the readout design does not require vias for charge evacuation from the DLC layers to the pads beneath the pillars, a feature needed only for high-rate configurations, which significantly simplifies manufacturing. Moreover, while typical pad sizes in non-capacitive Micromegas readouts are directly determined by the required spatial resolution (often in the range of 1–2 mm pitch to achieve sub-millimetre resolution), the capacitive-sharing approach allows for larger readout pad (5–10 mm) without sacrificing spatial resolution, as shown in section 4.2.

The choice of a 2D readout based on pads or X/Y strips (or X/U/V with stereo views) depends on the detector requirements, including spatial resolution, rate capability, reconstruction robustness, ghost rejection, and acceptable noise levels. Pad readout offers greater geometrical flexibility, with adjustable granularity and pad size, and provides both coordinates on the same plane, thereby reducing ghost hits and enabling a straightforward implementation of capacitive charge sharing. In general, the pad geometry allows smaller electrodes, reducing occupancy and noise compared to long strips with similar spatial resolution, at the cost of more channels. In summary, the parameters guiding the choice between strip and pad readout, in a specific application, are: spatial resolution in both coordinates, number of channels, electrode dimensions, ghost rejections, occupancy and electronic noise.

3 Prototype characterisation with X-rays

The capacitive-sharing prototype was characterized by measuring its gain using X-rays from a ^{55}Fe radioactive source. The gas mixture used was Ar-CO_2-iC_4H_{10} (93-5-2), where the addition of 2% of isobutane to standard Ar-CO_2 mixtures provides higher gain with improved stability [5]. Throughout all measurements, the drift electric field was kept constant at 600 V/cm.

Figure 4 shows the ^{55}Fe energy spectrum measured with the Paddy-CS-S section of the prototype, operated at an amplification voltage of 500 V. The main photopeak at 5.9 keV and the argon escape peak at 2.7 keV are clearly visible. The energy resolution, defined as the ratio of the Full Width at Half Maximum (FWHM) to the centroid of the main photopeak (obtained from a Gaussian fit), was determined to be 17.5% at 5.9 keV.

The gain (G) was determined by measuring the detector current I_{amp} driven by the power supply across the amplification gap, at various amplification voltages and the X-ray interaction rate (R), using the following formula:

$$G = \frac{I_{\text{amp}}}{R \times N_p \times e} \tag{3.1}$$

where e is the elementary charge and N_p is the average number of electron-ion pairs produced per X-ray interaction with the gas molecules. The average value of N_p was estimated from simulations using Garfield++ [9] ($N_p = 211$ for the Ar-CO_2-iC_4H_{10} gas mixture). To minimize the uncertainty on the current I_{amp}, the value was determined by averaging approximately 100 measurements acquired at one-second intervals.

Figure 5 displays the gain curves as a function of the amplification voltage for both the Paddy-CS-L and Paddy-CS-S sections of the detector. The measurements extend up to the last stable point before onset of discharges. The detector demonstrates stable operation up to a gain of approximately 4×10^4

2026 JINST 21 P03017

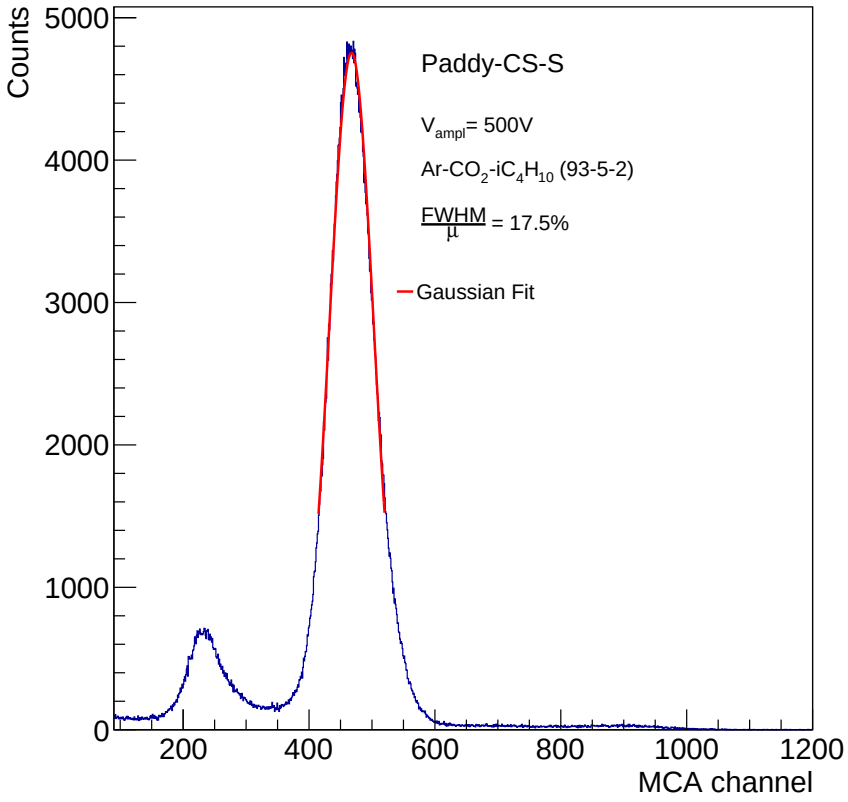

Figure 4. ^{55}Fe energy spectrum for Paddy-CS-S prototype.

for both sections. Measurements were taken under conditions in which the noise level, reduced through the optimization of the grounding configuration, was below a few percent of the main peak amplitude. Under these conditions, the spectral shape and the rate measurements were not significantly affected, as visible in figure 4, where the pedestal is not visible and lies below threshold.

4 Test-beam results

In April 2024, the prototype was tested using 150 GeV muon beams in the H4 SPS test beam area at CERN [10]. The layout of the test beam setup is shown in figure 6. The setup included a frame containing two scintillators for triggering (S1 and S2), two X-Y strip resistive Micromegas detectors providing external tracking (TMM-256), the capacitive-sharing chamber (Paddy-CS) and other Micromegas prototypes under test. Both TMM-256 detectors feature 256 strips per view with a pitch of 0.4 mm. The frame hosting the chambers allows the detectors under test to be inclined at angles between 0° and 40° with respect to the beam direction. The chambers were operated with either Ar-CO_2-iC_4H_{10} (93-5-2) or Ar-CF_4-iC_4H_{10} (88-10-2) gas mixtures; the latter benefits from faster electron drift, which can improve the time resolution. The signals were read out using the APV25 [11] front-end ASICs connected to the Scalable Readout System [12].

2026 JINST 21 P03017

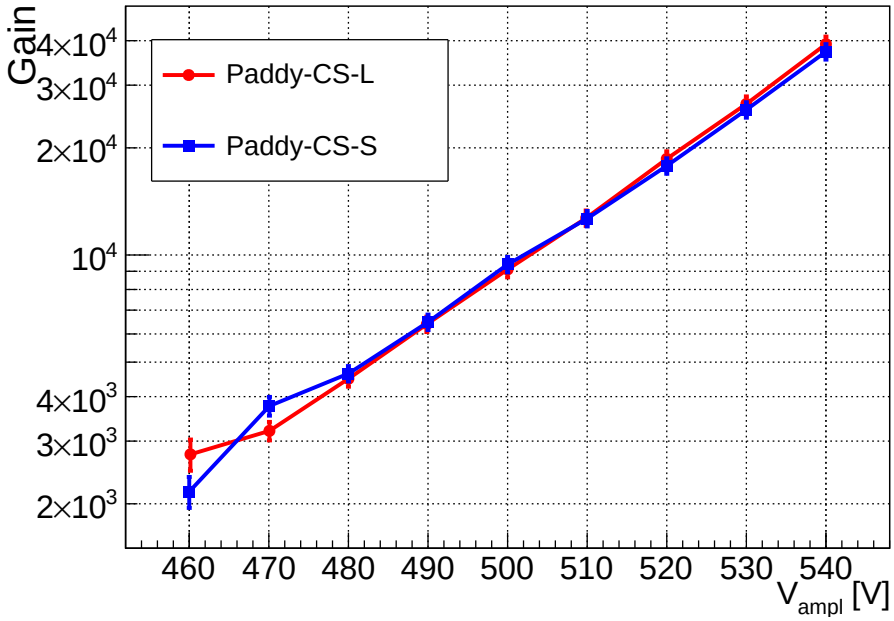

Figure 5. Gain as a function of the amplification voltage for Paddy-CS-L and Paddy-CS-S side of the capacitive-sharing prototype, operated with Ar-CO_2-iC_4H_{10} (93-5-2) gas mixture.

The reference coordinate system was defined with the z-axis along the incoming beam direction, the y-axis pointing vertically upward and the x-axis parallel to the ground. The chamber is set up with the x and y coordinates as shown in figure 2, where the edge shared between the two chamber sides is along the x-axis.

To obtain a clean sample of reference tracks, events were selected when exactly one cluster was reconstructed in both views of each TMM tracking chamber. From the measurements in the TMM chambers, a reference track was determined and interpolated to the position of the Paddy-CS to measure spatial resolution and efficiency. Detectors' relative positions and rotations were corrected offline using an iterative procedure based on the distribution of the track residuals as a function of the x and y coordinates.

Data were collected with the TMM reference chambers operated at their optimal working point, while the amplification voltage of the chamber under test was varied from 420 V to 550 V. The drift field was kept constant at 600 V/cm. To suppress the noise, a charge threshold was applied on each channel, set to seven times the RMS noise level (1 RMS $\simeq$ 0.4 fC).

4.1 Cluster charge, multiplicity and time

The time and charge of the pad were measured as follows: for every pad above threshold, the APV25 returns the shape of the charge-sensitive amplifier signal, sampled in 25 ns bins. The pad time and charge were then extracted by fitting the rising edge of the APV25 signal with a Fermi-Dirac function [13]. The pad time is defined as the time corresponding to the inflection point of the rising slope (i.e., the half-height of the Fermi-Dirac fit), while the charge is taken as the maximum of the Fermi-Dirac function.

2026 JINST 21 P03017

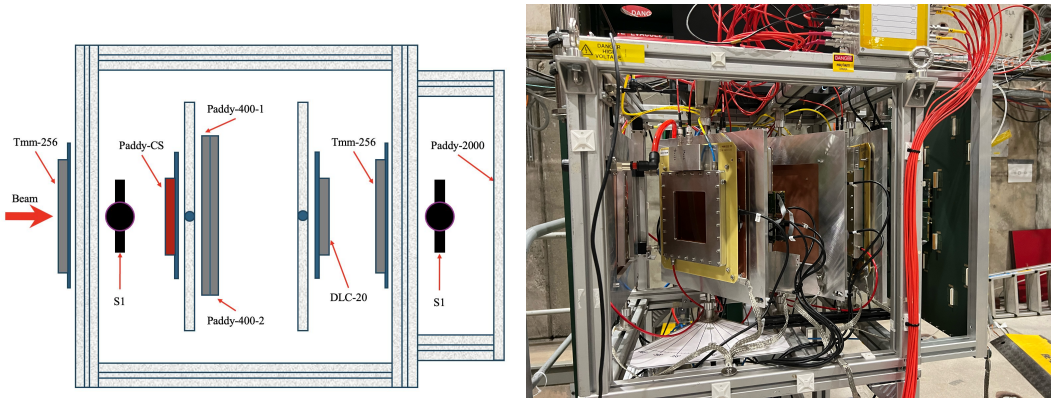

Figure 6. Layout of the Micromegas test beam setup containing the capacitive-sharing prototype (in red) under study. The Paddy-CS detector was positioned 150 mm downstream of the first TMM chamber and 340 mm upstream of the second TMM chamber. On the right a photo of the setup is also shown.

Clusters were reconstructed by combining adjacent fired pads. Figure 7 shows the Landau-shaped distributions of cluster charge measured with the Paddy-CS-L and Paddy-CS-S sides of the detector operated at 470 V and 460 V, for the two gas mixtures: Ar-CO_2-iC_4H_{10} (93-5-2) and Ar-CF_4-iC_4H_{10} (88-10-2). The distributions are fitted with Landau functions, and the most probable value (MPV) was extracted for each configuration. When operated with a 10 V difference in amplification voltage, the mean and MPV values for the two gas mixtures are comparable, indicating a similar detector response. The decrease in cluster charge in the Side-S section compared to Side-L is likely due to weaker capacitive coupling among pads of the same size, in contrast to the coupling between pads of increasing size. A similar behaviour is measured at each gain value. Simulation studies are currently underway to further investigate this effect.

Figure 8 shows the average number of pads per cluster for both Paddy-CS-L and Paddy-CS-S sides as a function of the amplification voltage, for the two gas mixtures used. The measurements were performed using tracks perpendicular to the detector plane. The x and y projections are shown separately along with the total 2-dimensional cluster size. As observed in figure 8, the mean number of pads per cluster ranges from 2 up to 22 (for Paddy-CS-S) and up to 13 (for Paddy-CS-L) at high amplification voltage. The cluster size impacts the precision of the cluster position measurement, and thus the spatial resolution. A multiplicity greater than two pads ensures a good position resolution performance, as shown in the following sections. It can be observed that the cluster-size projected along the x coordinate is systematically larger than the projection along the y coordinate, with a modest difference (below 10%) at nominal operation conditions ($V_{\text{ampl}} \simeq 500$ V — Gain $\simeq 10^4$) and growing with the gain. This directional asymmetry is attributed to cross-talk effects caused by the routing traces present in the multilayer PCB structure, shown in figure 2, that run along the x direction. This directional cluster broadening along x degrades the position measurement accuracy, systematically resulting in projected spatial resolutions along x that are worse than those obtained along the y-coordinate, as detailed in section 4.2. One possible explanation for the large number of pads in a cluster, which increases with detector gain, is that crosstalk between adjacent pads plays a role. In the first layer, which is closer to the amplification gap and features smaller pads, the distance between adjacent pads is only 50 µm. At such a small separation, capacitive coupling between neighbouring pads can be significant. This effect, together with the previously mentioned mechanism leading to larger clusters in the x-coordinate, will be further investigated.

2026 JINST 21 P03017

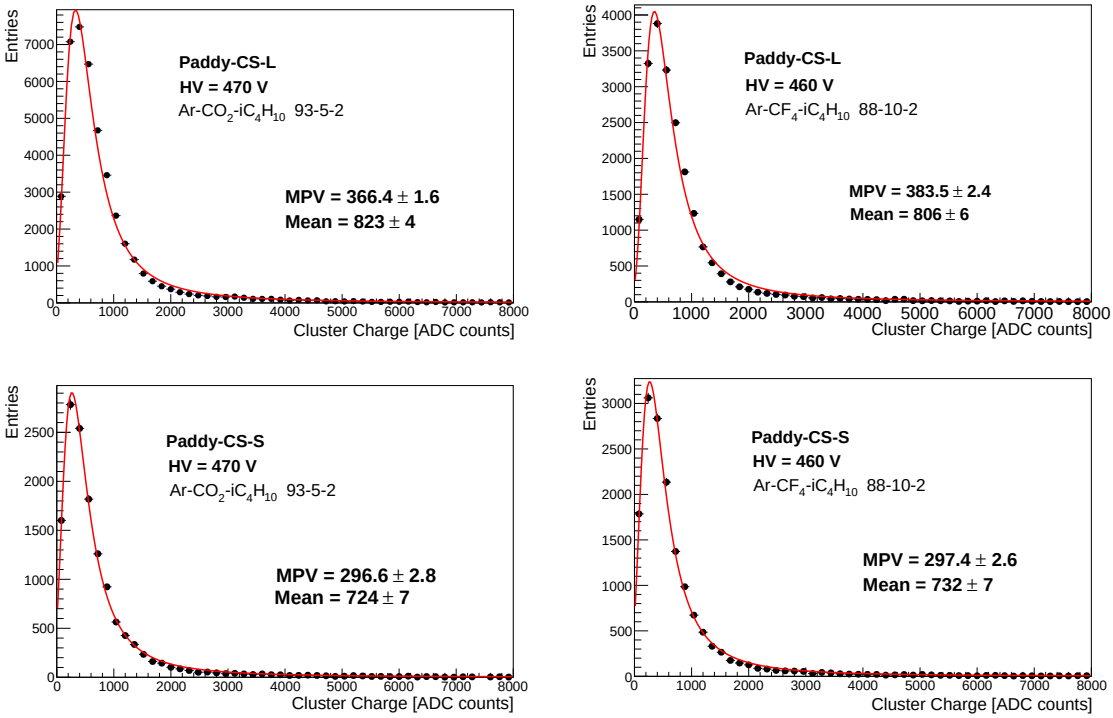

Figure 7. Cluster charge distributions for the two detector sides and for the Ar-CO_2-iC_4H_{10} (93-5-2) and Ar-CF_4-iC_4H_{10} (88-10-2) gas mixtures. A fit with a Landau distribution is shown as a superimposed line.

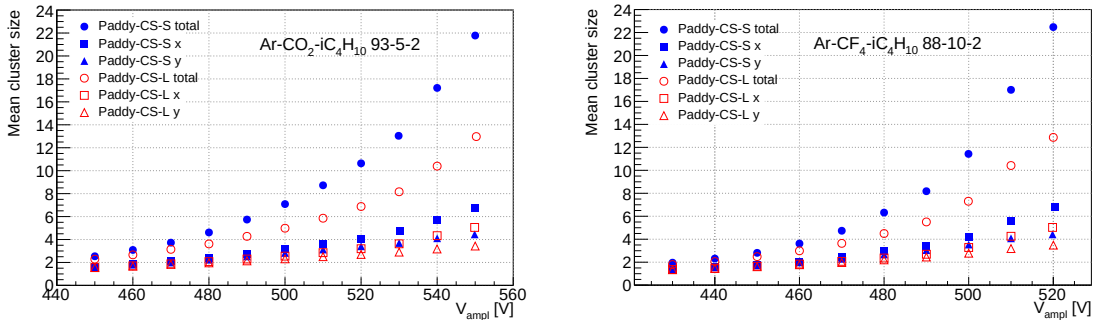

Figure 8. Average number of pads per cluster as a function of the applied amplification voltage for data taken with the Ar-CO_2-iC_4H_{10} (93-5-2) gas mixture (left) and the Ar-CF_4-iC_4H_{10} (88-10-2) gas mixture (right).

4.2 Spatial and time resolution

The spatial resolution of the detector was first determined using perpendicular tracks, by measuring the width of the distribution of cluster position residuals with respect to the extrapolated track position, reconstructed from the TMM chambers. The extrapolation uncertainty, approximately 50 µm, was subtracted in quadrature from the measured resolutions.

2026 JINST 21 P03017

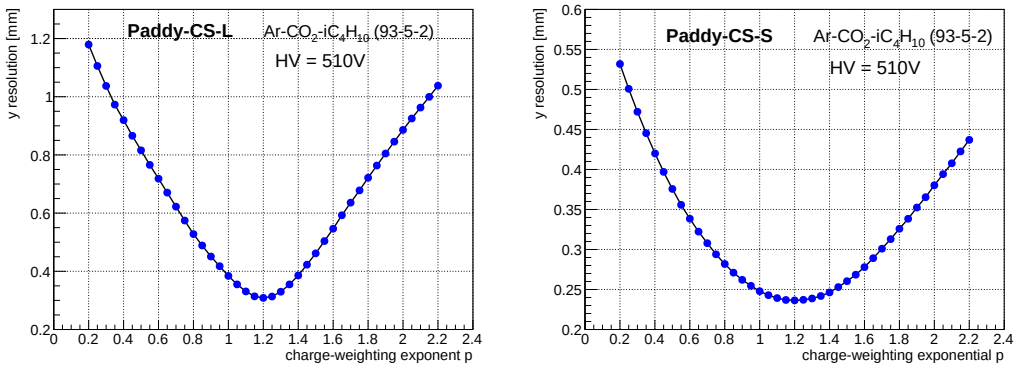

Figure 9. Spatial resolutions in the y coordinates, for perpendicular tracks, as a function of the charge-weighting parameter p, for the Paddy-CS-L (left) and Paddy-CS-S (right) detector sides. Data with the Ar-CO_2-iC_4H_{10} (93-5-2) gas mixture taken with an amplification voltage of 510 V are shown.

The cluster position was evaluated along both coordinates with an extended definition of the charge-weighted centroid:

$$x_c = \frac{\sum x_i (Q_x)_i^p}{\sum (Q_x)_i^p} \quad ; \quad y_c = \frac{\sum y_i (Q_y)_i^p}{\sum (Q_y)_i^p} \tag{4.1}$$

where x_i (y_i) is the position at the i-th x-coordinate (i-th y-coordinate) and

$$Q_x = \sum_y q_{xy} \quad ; \quad Q_y = \sum_x q_{yx} \tag{4.2}$$

are the total charges measured at fixed x_i (summing over all q_y along the y-coordinate) and at fixed y_i (summing over all q_x along the x-coordinate), respectively.

The parameter p, usually set to 1, was instead optimised by minimising the residuals. The optimisation procedure is illustrated in figure 9, which shows the scan of the y residual widths as a function of the parameter p for both sides of the detector at an amplification voltage of 510 V and for the Ar-CO_2-iC_4H_{10} (93-5-2) gas mixture. The optimal value was found to be $p = 1.2$ for both sides and views of the detector, for all amplification voltages and different gas mixtures. The corresponding resolutions are shown in figure 10 as a function of the amplification voltage. Spatial resolution is defined as the half-width of the central interval of the residual distribution containing 68% of the events, which corresponds to one standard deviation for a Gaussian distribution. Resolutions with non-optimised centroid ($p = 1$) are also shown for comparison.

As seen in figure 10, the optimised centroid improves the spatial resolution, particularly for the Paddy-CS-L side, where improvements up to 20% are observed. The degradation of resolution observed at high amplification voltages is attributed to charge saturation effects in the APV25 readout electronics, which distort the charge-weighted centroid calculation. The spatial resolution obtained along the x-coordinate is systematically worse than the resolution achieved along the y-coordinate for both detector sections (Paddy-CS-L and Paddy-CS-S). This directional difference is a direct consequence of the cross-talk along the x-axis, caused by the routing traces present in the inner layers of the PCB, as discussed in section 4.1. Figure 11 shows the residual distributions at the optimal amplification voltage for both detector sides in the y-coordinate view. At the optimal amplification voltage working point,

2026 JINST 21 P03017

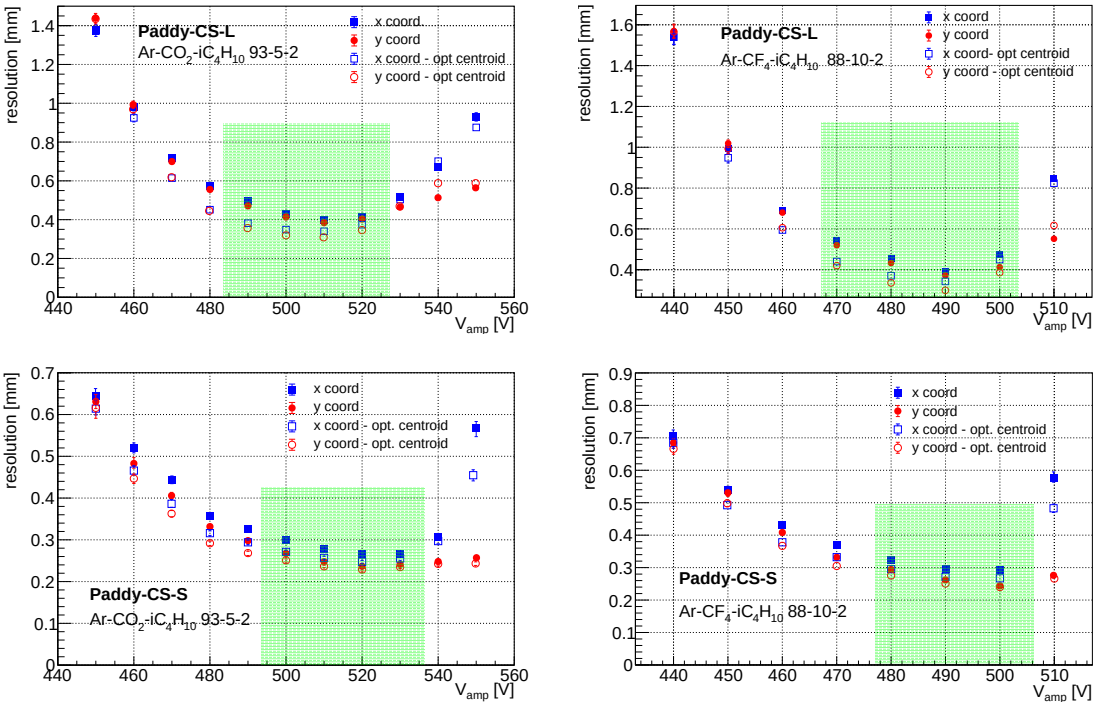

Figure 10. Spatial resolutions, for perpendicular tracks, in both x and y coordinates, as a function of the amplification voltage, for the Paddy-CS-L (top) and Paddy-CS-S (bottom) detector sides. Data with both the Ar-CO_2-iC_4H_{10} (93-5-2) (left) and Ar-CF_4-iC_4H_{10} (88-10-2) (right) gas mixtures are shown. Resolutions are shown with and without centroid optimization. Only statistical uncertainties are considered. The shaded green area indicates the voltage range corresponding to optimal spatial resolution performance.

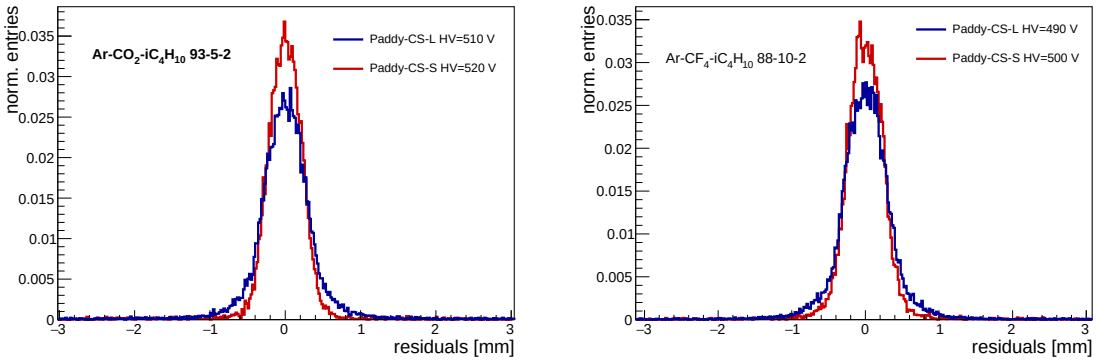

Figure 11. Distribution of the residuals, for perpendicular tracks and after charge centroid optimisation, in the *y*-coordinate for Paddy-CS-L and Paddy-CS-S at optimal amplification voltage for both the Ar-CO_2-iC_4H_{10} (93-5-2) (left) and the Ar-CF_4-iC_4H_{10} (88-10-2) (right) gas mixtures.

spatial resolutions of approximately 250 µm for the Paddy-CS-S side and 320 µm for Paddy-CS-L side are achieved, corresponding roughly to a factor 1/20 and 1/30 of the linear pad dimensions.

The spatial resolution of the Paddy-CS chamber was further studied with inclined tracks. Data were collected with the chamber rotated by approximately 38° relative to the beam direction, such that

2026 JINST 21 P03017

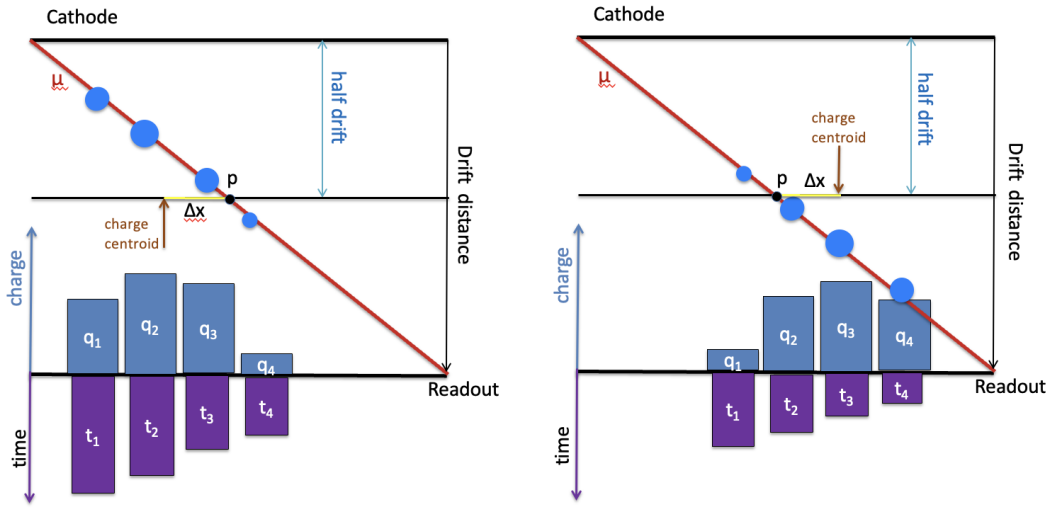

Figure 12. Schematic illustration of the CTP principle. Δx denotes the offset between the cluster position obtained with the charge-centroid algorithm and the true particle position at the centre of the drift gap. The blue and purple bars on the readout plane represent, respectively, the collected charge and the associated drift time. Two extreme scenarios are shown: on the left, only late clusters generate signals, whereas on the right, only early clusters do. In the first case (left), a shift toward smaller x values correlates with a larger cluster time; in the second case (right), a shift toward larger x values is associated with a shorter cluster time.

the x coordinate is affected, while negligible effects are expected on the y coordinate. For inclined tracks, the centroid method loses precision because the ionisations no longer occur at approximately the same coordinate but are instead distributed along the track path. Fluctuations in ionisation and charge multiplication lead to uneven charge sharing among pads, which biases the reconstructed position toward areas of higher charge deposition.

Standard methods to improve spatial resolution in MPGDs for inclined tracks have been developed by exploiting the time information from the strips or pads in a cluster. The micro Time Projection Chamber μTPC [13] and Cluster Time Projection (CTP) [14] techniques are notable examples. While the μTPC method reconstructs the cluster position by determining the track inside the drift gap, both in position and angle, the CTP correction instead requires the track angle to be known in advance. In this work, we focused on the CTP correction method, which is robust and easy to apply, particularly in cases with a limited number of strips or pads per cluster. The potential of the μTPC method will be explored in future studies.

The CTP method is illustrated in figure 12. It relies on the fact that a fluctuation of the cluster time towards earlier (or later) values relative to the "central" cluster time, defined as the time corresponding to a charge deposition produced at half of the drift gap along the particle track (denoted as p in figure 12), is strongly correlated with a negative (or positive) position bias of the cluster centroid. This method is exploited to improve the resolution for inclined tracks. The centroid positions are corrected using the correlation between the spatial shift of the reconstructed position and the charge-weighted average of the signal arrival times of the pads forming the cluster:

$$t_{cl} = \frac{\sum t_i q_i}{\sum q_i} \tag{4.3}$$

2026 JINST 21 P03017

where t_i and q_i are the signal arrival time and the charge of the i-th pad, respectively. Figure 13 shows the correlation between the residuals obtained with the charge centroid method and t_{cl}, which, as expected, exhibits a linear dependency that is exploited to correct the cluster position.

As stated before, the CTP correction depends on the incident angle, known in this particular case, but that, in general, needs to be estimated with an independent method.

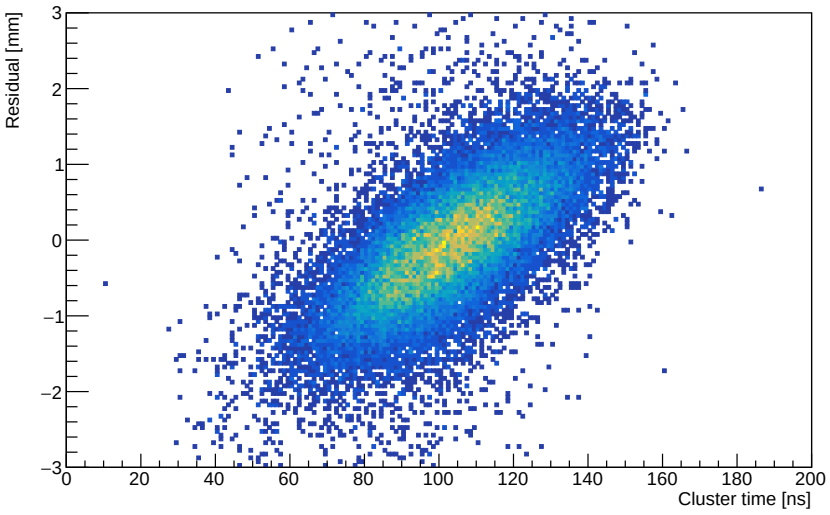

Figure 13. Charge centroid Residuals as a function of the charge-weighted average cluster time of the pads in a cluster.

Figure 14 shows the distribution of the residuals at amplification voltage of 490 V of the Paddy-CS-L side before and after the CTP correction. Figure 15 shows the spatial resolution of Paddy-CS-L side as a function of the amplification voltage with no correction applied, with only the spatial centroid optimisation applied, with only the CTP correction applied, and with all the corrections applied. It can be seen that the main improvement is provided by the CTP method. An overall improvement of about 40% is observed and the optimal resolution is below 500 µm. For inclined tracks, the Paddy-CS-S side resolutions are not analysed since this part of the detector was out of acceptance after the rotation. The successful application of the CTP method suggests that the capacitive-sharing technique preserves the information of the arrival times of the electrons induced signals on the readout pads, although cross-talk and pile-up of the arrival times on adjacent pads may potentially spoil the timing resolution.

The time resolution was directly analysed using the Ar-CO_2-iC_4H_{10} (93-5-2) gas mixture, with a drift field of 600 V/cm, corresponding to a drift velocity of approximately 4.5 cm/µs. For each cluster, the cluster time was defined as the average time of all hits belonging to the cluster. In order to minimize the impact of multiple primary ionizations on a single pad, the analysis was performed using tracks inclined of 38° with respect to the beam direction. The time resolution was extracted from the distribution of the difference between cluster times measured in two detectors crossed by the same track. First, the time difference between two Paddy-400 chambers operated in the same test beam setup was analysed. The two Paddy-400 detectors were mounted in a sandwich configuration with a common cathode, as shown in figure 6. This configuration allows a precise relative timing comparison under identical operating conditions. The corresponding distribution was fitted with a

2026 JINST 21 P03017

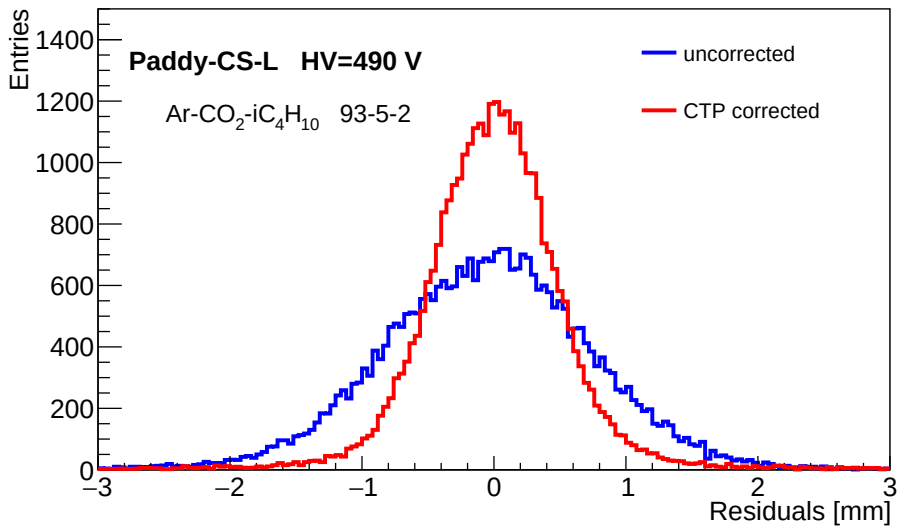

Figure 14. Distributions of the residuals, for inclined tracks at an angle of 38°, at amplification voltage of HV = 490 V, without and with the CTP correction for Paddy-CS-L.

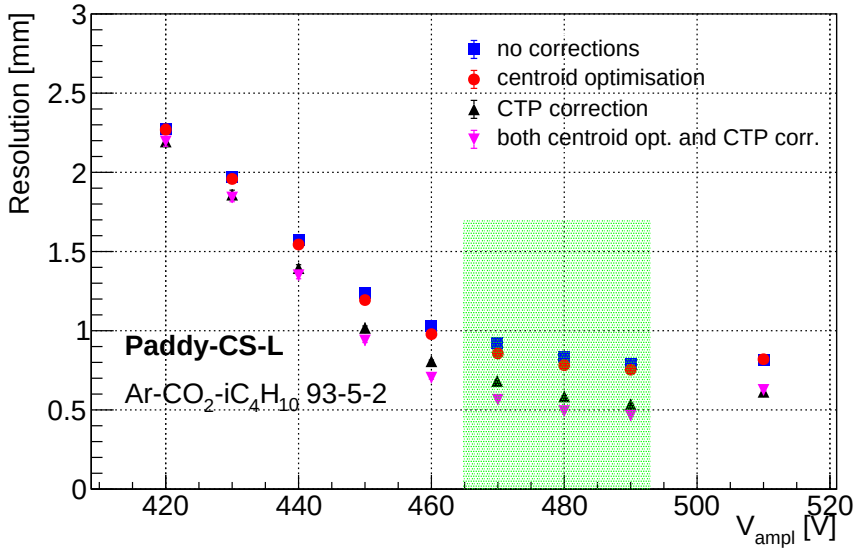

Figure 15. Paddy-CS-L spatial resolution, for inclined tracks at 38°, as a function of the amplification voltage for not optimised centroid (blue squared dots), after the spatial centroid optimisation (red dots), after CTP correction (black upward-pointing triangles) and after applying all the corrections (magenta downward-pointing triangles). Only statistical uncertainties are considered. The chamber is operated with the Ar-CO_2-iC_4H_{10} (93-5-2) gas mixture. The shaded green area indicates the voltage range corresponding to optimal spatial resolution performance.

Gaussian function, and the standard deviation of the fit, divided by $\sqrt{2}$, was taken as the reference timing resolution of the Paddy-400 system. The measured value is 13.2 ns, compatible with the time resolution previously reported for Paddy-400 detectors [4]. In a second step, the same analysis was applied to the time difference between the Paddy-CS-L detector and a Paddy-400 chamber. The intrinsic time resolution of the Paddy-CS-L detector was then obtained by subtracting in quadrature the previously measured Paddy400-Paddy400 contribution from the measured Paddy-CS-L — Paddy-400 width. The APV25 sampling clock (25 ns) is synchronous for all channels and therefore cancels out in the time difference measurement. The cluster time difference distribution and the corresponding Gaussian fit is shown in figure 16. A time resolution of 15.8 ns is measured, in good agreement with the performance previously reported for Paddy-400 detectors [4].

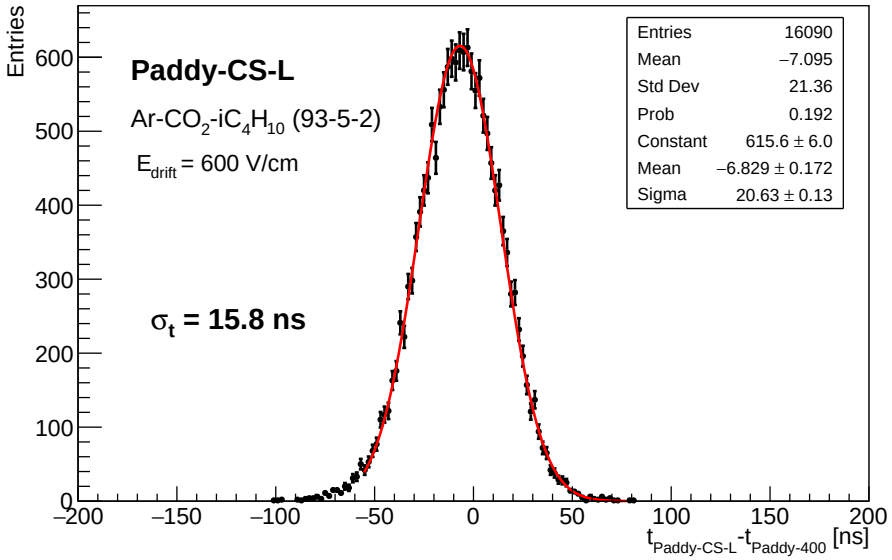

Figure 16. Distributions of the average cluster time differences between Paddy-CS-L and Paddy-400 detectors, for inclined tracks at an angle of 38°, operated at amplification voltage of HV = 470 V, electric drift field of E_{drift} = 600 V/cm in Ar-CO_2-iC_4H_{10} (93-5-2) gas mixture.

4.3 Efficiency

Efficiency was assessed initially using tracks perpendicular to the detector plane. Detection efficiency is defined as the ratio between the number of extrapolated reference tracks whose projected position is either geometrically inside a reconstructed cluster or within a distance equal to half the readout pad size from it, and the total number of extrapolated tracks. Figure 17 (left) shows the efficiencies as a function of the amplification voltage for the Ar-CF_4-iC_4H_{10} (88-10-2) gas mixture. The efficiency plateau is approximately 98%. The remaining 2% inefficiency is mainly due to dead zones in the pillar positions, where no charge is collected and thus clusters cannot be reconstructed. This is illustrated in figure 17 (right), which shows the two-dimensional efficiency map for the Paddy-CS-S side operated at 480 V. An inefficiency is observed in correspondence of the support pillar positions, while elsewhere it remains close to 100%.

2026 JINST 21 P03017

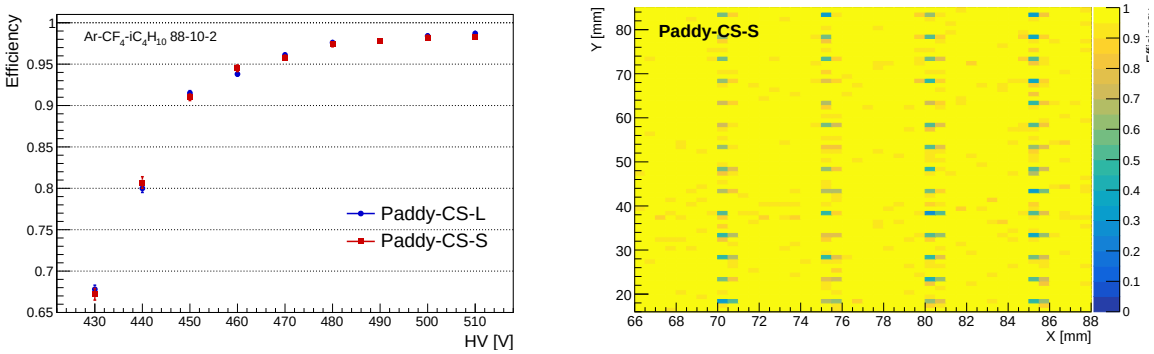

Figure 17. Efficiency, for perpendicular tracks, as a function of the amplification voltage for Paddy-CS-L and Paddy-CS-S for data collected with Ar-CF_4-iC_4H_{10} (88-10-2) gas mixture (left). Two dimensional efficiency in the Paddy-CS-S detector side at amplification voltage of 480 V (right).

The efficiency in the Paddy-CS-L side was also measured with inclined tracks, with the chamber rotated by about 38° with respect to the beam direction. In this configuration, the impact of the support pillars is expected to be reduced, as inclined tracks are more likely to produce ionisation across areas larger than the pillar dimensions. Figure 18 (left) shows the efficiency as a function of the amplification voltage for data taken with the Ar-CO_2-iC_4H_{10} (93-5-2) gas mixture, reaching a plateau above 99%.

In figure 18 (right), the two-dimensional efficiency map clearly shows that the average increase of efficiency with respect to perpendicular tracks, since the drop due to the pillars is no longer visible. The central white region in the efficiency map corresponds to an acceptance cut applied to exclude two noisy channels.

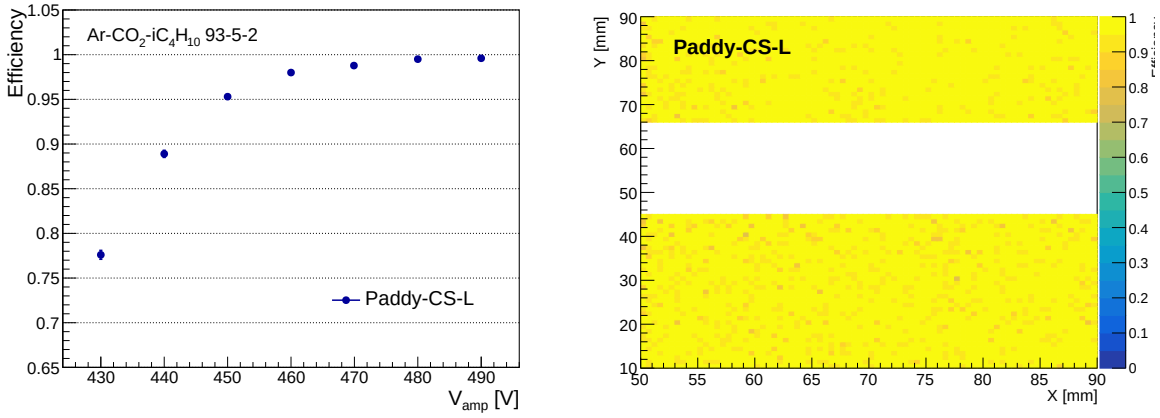

Figure 18. Paddy-CS-L efficiency, measured with inclined tracks, as a function of the amplification voltage (left) and as a function of the x-y coordinates (right) for an amplification voltage of 490 V. Data were taken with the Ar-CO_2-iC_4H_{10} (93-5-2) gas mixture. The central white region in the efficiency map corresponds to an acceptance cut applied to exclude two noisy channels.

2026 JINST 21 P03017

5 Conclusions

Micro-pattern gaseous detectors (MPGDs) are increasingly used in high-energy and nuclear physics experiments for their high spatial resolution and reliability. However, while their segmented readout improves precision, it complicates large-scale integration due to the increased complexity, number of electronic channels, and overall cost. Overcoming these challenges is essential for future applications.

Capacitive-sharing readout is a novel concept designed to exploit PCB designs with coarser readout segmentation, significantly reducing the number of channels and thus the cost of electronics. This approach allows the development of cost-effective, large-area tracking detectors with fewer readout channels, while preserving excellent spatial resolution. It is particularly well suited for future experiments at FCC-ee, where high rate capability is not a primary requirement.

In this paper, we presented the performance of a resistive Micromegas prototype with capacitive-shared pad readout, developed in collaboration with the CERN MPT workshop group. Stable operations were achieved up to an amplification voltage of 540 V with gains around 4×10^4. A detector efficiency above 98% was measured. With perpendicular tracks, a spatial resolution performance of approximately 250 µm was obtained for readout pads with a pitch of $5 \times 5\,\mathrm{mm}^2$, corresponding to 1/20 of the pad pitch and requiring only 1/16 of the readout channels compared to a fully instrumented readout layer with $1.25 \times 1.25\,\mathrm{mm}^2$ pads (as used in the innermost layer). For larger readout pads, with a pitch of $10 \times 10\,\mathrm{mm}^2$, a spatial resolution of around 320 µm was achieved, corresponding to 1/30 of the pad size, while using only 1/64 of the channels. With inclined tracks, at 38°, a resolution below 500 µm was reached for $10 \times 10\,\mathrm{mm}^2$ readout pads. Dedicated methods were developed to improve the cluster reconstruction, optimising the charge-weighted centroid for position determination and using signal arrival time information for inclined tracks.

New prototypes are currently under development to further measure the performance of the capacitive-sharing readout for Micromegas. This ongoing R&D effort includes the realisation of large area detectors and different/optimised readout schemes and geometries.

Recent advances in resistive Micromegas, implementing the capacitive-sharing readout concept, make this technology a strong MPGD candidate for future HEP applications, including muon system detectors in the different FCC detector concepts.

Acknowledgments

We would like to thank the CERN MPT workshop and in particular R. De Oliveira and his team, for their ideas, discussions, and construction of the detectors. The authors also thank E. Oliveri and the entire DRD1 (former RD51) Collaboration for their support during the tests at the Gas Detector Development (GDD) Laboratory and during the test beam at CERN.

References

[1] Y. Giomataris, P. Rebourgeard, J.P. Robert and G. Charpak, *MICROMEGAS: A high granularity position sensitive gaseous detector for high particle flux environments*, *Nucl. Instrum. Meth. A* **376** (1996) 29.

[2] T. Alexopoulos et al., *A spark-resistant bulk-micromegas chamber for high-rate applications*, *Nucl. Instrum. Meth. A* **640** (2011) 110.

[3] M. Alviggi et al., *Construction and test of a small-pad resistive Micromegas prototype*, 2018 *JINST* **13** P11019.

2026 JINST 21 P03017

[4] M. Alviggi et al., *Resistive fine granularity Micromegas: characterization and performance for different spark protection resistive schemes*, 2025 *JINST* **20** P01012 [arXiv:2411.17202].

[5] ATLAS Muon collaboration, *Test of ATLAS Micromegas detectors with ternary gas mixture at the CERN GIF++ facility*, *PoS* **EPS-HEP2021** (2022) 757.

[6] G.F. Knoll, *Radiation Detection and Measurement*, 4th edition, John Wiley & Sons, Inc. (2010) ISBN: 978-0-470-13148-0.

[7] K. Gnanvo, N. Liyanage, B. Mehl and R. de Oliveira, *Performance of a resistive micro-well detector with capacitive-sharing strip anode readout*, *Nucl. Instrum. Meth. A* **1047** (2023) 167782.

[8] I. Giomataris et al., *Micromegas in a bulk*, *Nucl. Instrum. Meth. A* **560** (2006) 405 [physics/0501003].

[9] Garfield++, https://garfieldpp.docs.cern.ch/.

[10] D. Banerjee et al., *The North Experimental Area at the CERN Super Proton Synchrotron*, CERN-ACC-NOTE-2021-0015, CERN (2021).

[11] M.J. French et al., *Design and results from the APV25, a deep sub-micron CMOS front-end chip for the CMS tracker*, *Nucl. Instrum. Meth. A* **466** (2001) 359.

[12] S. Martoiu, H. Muller, A. Tarazona and J. Toledo, *Development of the scalable readout system for micro-pattern gas detectors and other applications*, 2013 *JINST* **8** C03015.

[13] T. Alexopoulos et al., *Performance studies of resistive-strip bulk micromegas detectors in view of the ATLAS New Small Wheel upgrade*, *Nucl. Instrum. Meth. A* **937** (2019) 125.

[14] B.M. Flierl, *Particle Tracking with Micro-Pattern Gaseous Detectors*, Ph.D. thesis, Munich University, Munich, Germany (2018), http://nbn-resolving.de/urn:nbn:de:bvb:19-221980.

2026 JINST 21 P03017